JGR Solid Earth

RESEARCH ARTICLE
10.1029/2023JB026710

Deuterium Content and Site Occupancy in Iron Sulfide at High Pressure and Temperature Determined Using In Situ Neutron Diffraction Measurements

Sumith Abeykoon[1,2], Christopher Howard[1,3], Serena Dominijanni[1,4], Lisa Eberhard[1,5], Alexander Kurnosov[1], Daniel J. Frost[1], Tiziana Boffa Ballaran[1], Hidenori Terasaki[6], Tatsuya Sakamaki[7], Akio Suzuki[7], Eiji Ohtani[7], Asami Sano-Furukawa[8], and Jun Abe[9]

[1]Bayerisches Geoinstitut, University of Bayreuth, Bayreuth, Germany, [2]Now at Centre de Recherches Pétrographiques et Géochimiques, 7358 CNRS-UL 15 rue Notre Dame des Pauvres 54500, Vandoeuvre-lès-Nancy, France, [3]Now at ISIS Neutron and Muon Facility, Rutherford Appleton Laboratory, Oxfordshire, UK, [4]Now at Institut de Minéralogie de Physique des Matériaux et de Cosmochimie (IMPMC), Sorbonne Université, Muséum National d'Histoire Naturelle, CNRS, Paris, France, [5]Now at Department of Earth Sciences, Utrecht University, Utrecht, The Netherlands, [6]Department of Earth Sciences, Okayama University, Okayama, Japan, [7]Department of Earth and Planetary Material Sciences, Tohoku University, Sendai, Japan, [8]J-PARC Center, Japan Atomic Energy Agency, Tokai, Naka, Ibaraki, Japan, [9]Neutron Science and Technology Center, Comprehensive Research Organization for Science and Society, Tokai, Naka, Ibaraki, Japan

Abstract We have performed in situ time-of-flight neutron diffraction experiments to examine the uptake of deuterium in iron monosulfide at pressures up to 11.4 GPa and temperatures to 1300 K. A D_2 fluid was formed in the experiments through the decomposition of ND_3BD_3, resulting in an oxygen fugacity of approximately 1.2 log units below the iron-wüstite buffer. Deuterium positions and site occupancies were determined in FeS V, using Rietveld refinements of the powder neutron diffraction patterns. Our structural model indicates that two normally unoccupied sites in the $P6_3/mmc$ FeS V structure, at Wyckoff positions *6h* and *4f*, are partially occupied by D atoms, with the latter being more dominant. The deuterium content D_x in $FeSD_X$ increases with both pressure and temperature over the experimental conditions explored, from 0.126 (14) at 2.3 GPa and 787 K to 1.20 (16) at 9.7 GPa and 1300 K. The unit-cell volume expansion per deuterium atom is 1.53 ± 0.16 Å^3 at 6.9 GPa and 960 K, which is smaller than that determined for metallic iron phases at similar conditions. The variation in unit-cell volume indicates that most deuterium is lost from FeS V upon temperature quenching at high-pressures. By fitting the obtained FeS V deuterium site occupancies to a thermodynamic model, estimates for the hydrogen contents of iron monosulfide at conditions and oxygen fugacities consistent with the base of the cratonic lithosphere can be made. This results in values in the range of 1,700–2,700 ppm, which contribute to approximately 2–3 ppm hydrogen in the bulk mantle.

Plain Language Summary Small amounts of iron sulfide minerals are found in most rocks from the Earth's mantle and as inclusions trapped in natural diamonds. Hydrogen may dissolve into iron sulfide minerals under high pressures and temperature, but is most likely lost once pressure and temperature are removed. In this study, we determined deuterium contents (deuterium was used as a proxy for hydrogen as it has better neutron scattering properties) in iron sulfide, held under high pressure and temperature conditions, using neutron diffraction measurements. Our results show that the amount of deuterium in iron sulfide increases with both pressure and temperature, but the deuterium is lost on recovery to room conditions. The results are used to estimate hydrogen contents of iron sulfide minerals in the deep continental lithospheric mantle, which are found to be in the range 1,700–2,700 ppm. This corresponds to approximately 2–3 ppm of hydrogen in the bulk mantle.

Key Points:

- Deuterium contents in iron sulfide were measured at high-*P*, up to 11.4 GPa and high-*T* to 1300 K in in situ neutron diffraction experiments
- The total deuterium content, D_x in $FeSD_X$, increases with both *P* and *T*, from 0.126 (14) at 2.3 GPa and 787 K to 1.20 (16) at 9.7 GPa and 1300 K
- A thermodynamic model shows that the hydrogen contents of iron monosulfide at the base of the cratonic lithosphere could be 1,700–2,700 ppm

Supporting Information:

Supporting Information may be found in the online version of this article.

Correspondence to:

S. Abeykoon,
sumith.abeykoon@uni-bayreuth.de

Citation:

Abeykoon, S., Howard, C., Dominijanni, S., Eberhard, L., Kurnosov, A., Frost, D. J., et al. (2023). Deuterium content and site occupancy in iron sulfide at high pressure and temperature determined using in situ neutron diffraction measurements. *Journal of Geophysical Research: Solid Earth*, *128*, e2023JB026710. https://doi.org/10.1029/2023JB026710

Received 12 MAR 2023
Accepted 26 AUG 2023

Author Contributions:

Conceptualization: Sumith Abeykoon, Daniel J. Frost, Tiziana Boffa Ballaran
Data curation: Christopher Howard, Serena Dominijanni, Alexander Kurnosov, Tiziana Boffa Ballaran, Hidenori Terasaki, Asami Sano-Furukawa
Formal analysis: Sumith Abeykoon
Funding acquisition: Daniel J. Frost

1. Introduction

Iron-nickel-rich mono-sulfides are found as accessory minerals in almost all mantle rocks; sulfide melts were also an important core-forming component during planetary differentiation (Harvey et al., 2016; O'Neill, 1991; Rubie et al., 2016). Based on the depression of the FeS melting point, and in situ X-ray diffraction measurements of the unit-cell volume of FeS mineral phases, it has been proposed that iron sulfide minerals and melts can both dissolve a significant concentration of hydrogen (Piet et al., 2021; Shibazaki et al., 2011). This might be relevant to a number of planetary scenarios. Recent analyses of InSight seismic measurements, for example, are consistent

Investigation: Sumith Abeykoon, Serena Dominijanni, Alexander Kurnosov, Daniel J. Frost, Tiziana Boffa Ballaran, Tatsuya Sakamaki, Akio Suzuki, Eiji Ohtani, Asami Sano-Furukawa
Methodology: Sumith Abeykoon, Christopher Howard, Serena Dominijanni, Lisa Eberhard, Daniel J. Frost, Tiziana Boffa Ballaran, Hidenori Terasaki, Tatsuya Sakamaki, Akio Suzuki, Asami Sano-Furukawa, Jun Abe
Supervision: Daniel J. Frost, Tiziana Boffa Ballaran
Writing – original draft: Sumith Abeykoon
Writing – review & editing: Christopher Howard, Serena Dominijanni, Lisa Eberhard, Alexander Kurnosov, Daniel J. Frost, Tiziana Boffa Ballaran, Akio Suzuki, Eiji Ohtani, Asami Sano-Furukawa, Jun Abe

with a lower than expected density for the Martian core (Stähler et al., 2021), too low, in fact, to be explained by the presence of sulfur as the only light alloying element, due to its limited cosmochemical abundance. This raises the possibility that hydrogen may also be present in a sulfur-rich Martian core (Urakawa et al., 2004). The highly siderophile element concentration of the Earth's mantle has been proposed to have also been established, in part, through the late-stage separation of iron sulfide-rich melt to the core (Kiseeva & Wood, 2013; Laurenz et al., 2016; O'Neill, 1991; Rubie et al., 2016; Wood & Halliday, 2005). If this melt were also to have removed hydrogen from an initially slightly water-bearing magma ocean, this might potentially explain how the Earth's mantle became more oxidized towards the end of core formation (Delano, 2001; Kasting, 1993), through the reaction (Ringwood, 1977; Sharp et al., 2013),

$$H_2O + 2FeO = Fe_2O_3 + H_2 \quad (1)$$

Furthermore, iron sulfide minerals and melts might be important hosts for hydrogen in the mantles of the Earth and other planetary bodies. As iron-rich sulfides are also common inclusions in diamonds, it is possible that they contain dissolved hydrogen that might influence their properties. To clarify these possibilities, it is necessary to examine how hydrogen partitions between sulfides and silicate or fluid phases under different mantle conditions, and most importantly under different oxygen fugacities.

A critical obstacle to the study of hydrogen in high-pressure and temperature fractionation processes, is that melt and mineral phases do not necessarily preserve hydrogen in quenched products recovered for analysis at ambient conditions. Mantle partial melt compositions, for example, can no longer be quenched to glasses in conventional high-pressure experiments performed above 3 GPa (Bondar et al., 2021; Tenner et al., 2009). This makes the analysis of hydrogen species unreliable because the quenched crystallized products might not retain the volatile inventory of the melt, either because the solubility is lower in the products or due to kinetic limitations causing fluid formation during quenching. This is compounded in studies on the behavior of hydrogen during core formation processes, because metallic iron-rich melts not only crystallize on quenching but hydrogen is also lost from the quenched metal and hydride phases during recovery to room pressure (Antonov et al., 1998; Fukai & Suzuki, 1986; Iizuka-Oku et al., 2017; Okuchi, 1997). Sulfide minerals and melts are likely similar in this respect and may not preserve their high-pressure and temperature hydrogen contents upon recovery to room temperature, at least above an as yet undetermined threshold.

There are several approaches that have been used to address the problem of hydrogen loss from metallic melts. Recent metal-silicate melt hydrogen partitioning experiments were performed with low bulk hydrogen contents (<1,000 wt. ppm H_2), assuming that the recovered quench-crystallized products retained hydrogen to ambient conditions, as a result of the concentrations being below the threshold where hydrogen would be lost from the products (Clesi et al., 2018; Malavergne et al., 2019). This may well be the case, but would be more convincing if the retention threshold were known and could be demonstrated to reproducibly preserve the melt concentration. Another possibility is to rapidly decompress and then quench hydrogen-bearing iron-liquids and estimate the initial hydrogen concentrations from the volume of the exsolved bubble network (Okuchi, 1997). This method suffers from some uncertainties that are hard to gauge, such as those arising from the exact conditions, and therefore gas volume, at which exsolution occurs or the possibility of hydrogen loss without bubble formation. A final possibility is to quench metallic liquids at high-pressures and determine the hydrogen contents through in situ methods before the pressure is removed (Tagawa et al., 2021). Such measurements use X-ray diffraction to estimate the metal hydrogen contents from the expansion in the unit-cell volume, compared to hydrogen-free samples. Because hydrogen is essentially invisible to X-rays, this requires a calibration, using an independent method, for the effect of hydrogen on the unit-cell volume of the solid phase in question.

From this discussion, it is clear that a first step in understanding the hydrogen contents of metal and sulfide liquids is to be able to determine the hydrogen concentrations of sub-solidus phases. This is also required for the thermodynamic treatment of the effect of hydrogen on melting and provides information on the potential storage of hydrogen by such phases in planetary mantles and inner cores. In this study in situ time-of-flight (TOF) neutron powder diffraction measurements have been performed on samples of $Fe_{(1-x)}S$ having the NiAs-type structure, (i.e., the FeS V structure as defined by Urakawa et al., 2004), at pressures between 2.3 and 11.4 GPa and temperature up to 1300 K, in order to quantify the position and solubility of deuterium in the crystal structure. $Fe_{(1-x)}S$ V, a polytype of pyrrhotite, remains the subsolidus mono-sulfide phase in the Fe–S system, throughout conditions of the upper mantle and transition zone (Shibazaki et al., 2011; Urakawa et al., 2004). The experiments

were performed in a multi-anvil press installed at the J-PARC spallation neutron source in Japan. Atomic positions and site occupancies of deuterium in the FeS V NiAs-type structure were determined through Rietveld structure refinements.

2. Materials and Methods

2.1. Sample Assemblage

High-pressure and temperature experiments were performed using two cubic assemblies with edge lengths (cubic edge length—CEL) of 15.0 and 10.5 mm, for experiments at $P \leq 7$ GPa and $P > 7$ GPa, respectively. The starting material was a cold pressed cylindrical pellet of FeS powder (99.9% pure troilite—from "Chempur") with a height of either 5 or 4 mm depending on the size of assembly used. This was placed between two deuterated ammonia borane (ND_3BD_3) pellets, either 1.0 or 0.7 mm thick, and loaded into a NaCl capsule, with an inner diameter of either 3 or 4 mm. The capsules were closed with a 1 mm thick disk of NaCl. The NaCl was also used for determining the experimental pressure at high *P-T*. The pellets of ND_3BD_3 undergo thermal decomposition into BN and D_2 ($ND_3BD_3 = BN + 3D_2$), upon heating above approximately 600–800 K at high-pressure (Nylén et al., 2009). The capsules contained approximately 18–23 mol % ammonia borane, which creates sufficient D_2 to saturate the FeS sample. Deuterium has a much higher scattering length/power (bound coherent scattering length = 6.67 fm) than hydrogen (−3.74 fm), and smaller incoherent scattering (Dawidowski et al., 2013; Sears, 1992), resulting in a better signal to noise ratio in the collected neutron diffraction patterns. At the same time, it is assumed that D and H have similar chemical behavior at high-pressure and high-temperature (Iizuka-Oku et al., 2017; Machida et al., 2014). NaCl is known to be an effective material for confining hydrogen at high *P* and *T* (Fukai et al., 2003; Machida et al., 2014; Sakamaki et al., 2009; Shibazaki et al., 2011). The capsules were placed inside a cylindrical graphite heater with graphite lids on the top and bottom, which in turn was inserted inside a cylindrical hole drilled at the center of a Cr_2O_3-doped MgO cube that served as a pressure transmitting medium. End caps, made out of ZrO_2 wrapped with molybdenum foil (for electrical conduction), were then placed in contact with both sides of the graphite resistance heater. The 15.0 and 10.5 mm CEL assemblies were compressed to target pressure between six tungsten carbide secondary anvils, with square truncations of edge lengths (TEL) 10 and 7 mm respectively. A diagram of the TEL 10 high-pressure cell assembly is shown in Figure S1 in Supporting Information S1.

2.2. High-Pressure and High-Temperature Neutron Diffraction

High-pressure and temperature time-of-flight neutron diffraction measurements were performed at the PLANET beamline (BL11) at the Material and Life Sciences Experimental Facility (MLF) in J–PARC, Japan (Hattori et al., 2015). The measurements were carried out using a six-ram multi-anvil high-pressure apparatus (ATSU-HIME), where the rams are aligned along three perpendicular compression axes. Each of the six rams is capable of applying a load of 5,000 kN (Sano-Furukawa et al., 2014) and is attached to an outer first-stage square faceted anvil. The rams are advanced simultaneously and compress an inner set of six square faceted second-stage tungsten carbide anvils, each inside a steal retaining ring. The second stage anvils are centered and initially held in place by an aluminum guide frame (see Iizuka-Oku et al., 2017 Supporting Information). To eliminate neutron scattering from the assembly materials surrounding the sample, a set of incident slits and two sets of receiving radial collimators (each aligned with the 90° diffraction geometry) are placed as close as possible to the gaps between the second stage anvils (Hattori et al., 2015). The radial collimators are aligned so that only neutrons diffracted within the sample region that are perpendicular to the incident beam can reach the detectors. The slit size/beam sizes are chosen based on the assembly size and pressure and are reported in Table 1. Diffracted neutrons were collected using two detector banks, 1.5 m from the beam axis, comprised of 160 individual ^{3}He position-sensitive detectors (Hattori et al., 2015).

A diffraction measurement was taken before compression of each experiment for 10 min to confirm that the incident neutron beam was aligned over the sample. Another diffraction pattern was collected after compression to the target pressure to (a) adjust any misalignment of the sample with respect to the neutron beam due to the compression of the whole assembly, (b) obtain diffraction from the NaCl pressure standard and (c) identify whether any phase transitions had occurred in the FeS sample during cold compression. Once the target pressure was reached, the sample was heated to the target temperature (Table 1) by supplying electrical power

Table 1
Summary of the Conditions at Which the Neutron Diffraction Experiments Were Performed and the Run Products Obtained During Compression, Heating and Decompression

Run #	TEL/CEL (mm)	Heater material	Slit size W × H (mm)	Starting materials	Max. *P* (GPa)	Max. *T* (K)	Time (hrs.)	Identified phases on heating/cooling path
A524-1	10/15	Graphite	2 × 5	FeS + ND_3BD_3	2.3 (2)	787	8	FeS I[a], IV[a], V
A524-2	10/15	Graphite	2 × 5	FeS + ND_3BD_3	2.7 (2)	940	7	FeS I[a], IV[a], V
A526	10/15	Graphite	2 × 4	FeS + ND_3BD_3	6.9 (4)	960	16	FeS I[b], IV[b], V
A593	7/10.5	Graphite	2 × 4	FeS + ND_3BD_3	9.7 (4)	1,300	19	FeS III[a], V + c BN[b]
A527[c]	7/10.5	TiC + Al_2O_3	2 × 4	FeS + ND_3BD_3	11.4 (5)	1,250	3	FeS V + c BN[b]
A595	7/10.5	Graphite	2 × 4	FeS	7.3 (4)	960	11	FeS III[a], V + Fe_3O_4 + Mo

Note. Some NaCl capsule material was identified in all the experiments. A524–1 and A524-2 are two data points collected for the same experiment at different *P*, *T* conditions (first high *T* measurement). TEL - truncation edge length, CEL - cube edge length. Neutron beam dimensions (slit sizes) are given as width (W) × height (H). Time refers to the total period over which the experiment was held at max *T*. At the *P* and *T* conditions reported for each experiment, the sample is FeS V phase. The other phases reported were either,

[a]Identified in the diffraction patterns acquired during compression (before heating). [b]Identified in the diffraction patterns acquired during cooling or decompression. [c]Blowout occurred.

to the heater and using a previously calibrated power-temperature relation (Figure S2 in Supporting Information S1). This calibration has been performed with a similar experimental set up but employing a type D ($W_{97}Re_3$–$W_{75}Re_{25}$) thermocouple (error ±50 K; Hernlund et al., 2006; Nishihara et al., 2020; Rubie, 1999). A total of six experiments were performed with pressures ranging from 2.3 to 11.4 GPa and temperatures between 787 and 1300 K (Table 1). Diffraction patterns were collected for up to 19 hr and were monitored during this time every 30–60 min. The long collection times were required to obtain a good signal to noise ratio, especially at higher pressures where the gap of the second stage anvils was smaller due to the higher load. All powder neutron diffraction patterns collected in this study at high *P*, *T* are shown in Figure S6 in Supporting Information S1, in addition to those shown in Figures 2 and 4.

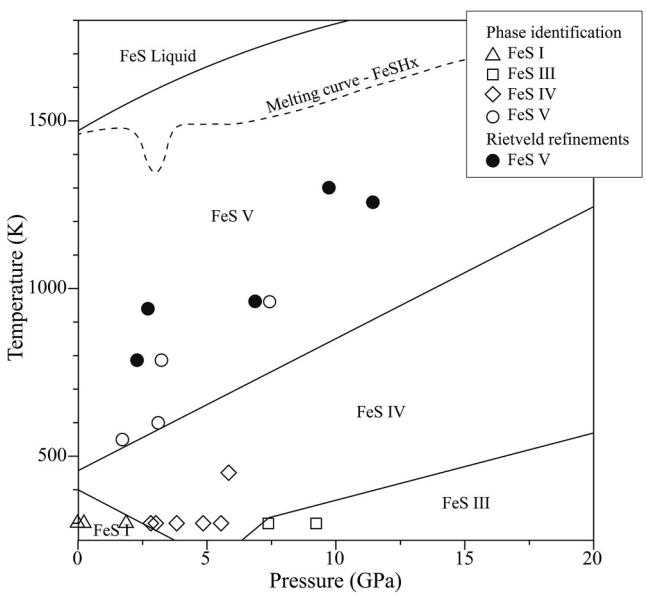

Figure 1. Observed high *P*, *T* polymorphs of FeS in this study (FeS I—triangles, FeS III—squares, FeS IV—diamonds and FeS V—circles) are shown on the existing phase diagram, where the solid lines show the phase boundaries from Urakawa et al. (2004). The dashed line shows the melting curve of $FeSH_X$ determined by Shibazaki et al. (2011). Filled circles (in the FeS V stability region) indicate the conditions where Rietveld refinements were performed to determine the deuterium site occupancy in FeS V. Open symbols indicate conditions where shorter diffraction measurements were performed for phase identification only. The FeS II (MnP-type orthorhombic) phase reported by Fei et al. (1995), is not shown here as it was not detected during our measurements. The unit-cell parameters of all observed phases are reported in Table S3 in Supporting Information S1.

2.3. Neutron Powder Diffraction Analysis

Intensity and background corrections were performed for all the collected diffraction profiles using the diffraction patterns of vanadium pellets and empty sample assemblies collected at the same conditions as those used for our measurements (see details in Hattori et al., 2015). A full profile analysis of the collected diffraction patterns was performed using the GSAS/EXPGUI software package (Larson & Von Dreele, 2004; Toby, 2001). Different FeS polymorphs (Table 1) were identified in the patterns collected during compression and decompression (Figure 1). Moreover, cubic boron nitride (c BN) is present in the diffraction patterns collected after cooling in the two experiments performed at the highest pressures. This is produced through the decomposition of ND_3BD_3 to BN + D_2 at high-temperature, and the stability of the cubic BN phase is consistent with the existing phase diagram (Solozhenko et al., 1999). Due to the smaller sample size of these two experiments, the top and the bottom of the sample, where the ND_3BD_3 pellet products resided, are also inside the neutron beam. Magnetite (Fe_3O_4) was observed in the experiment conducted without deuterium (blank experiment). This mineral formed during the experiment, likely due to the more oxidizing conditions, compared to the deuterated experiments, that arise due to the presence of small amounts of adsorbed water in the assembly and starting materials. At the target *P*, *T* conditions (Table 1), we observed the presence of FeS V, in agreement with previously reported phase diagrams (Fei et al., 1998; Kusaba et al., 1998; Shibazaki et al., 2011; Urakawa et al., 2004) (Figure 1). Also, the phases identified during the heating and cooling path agree with existing

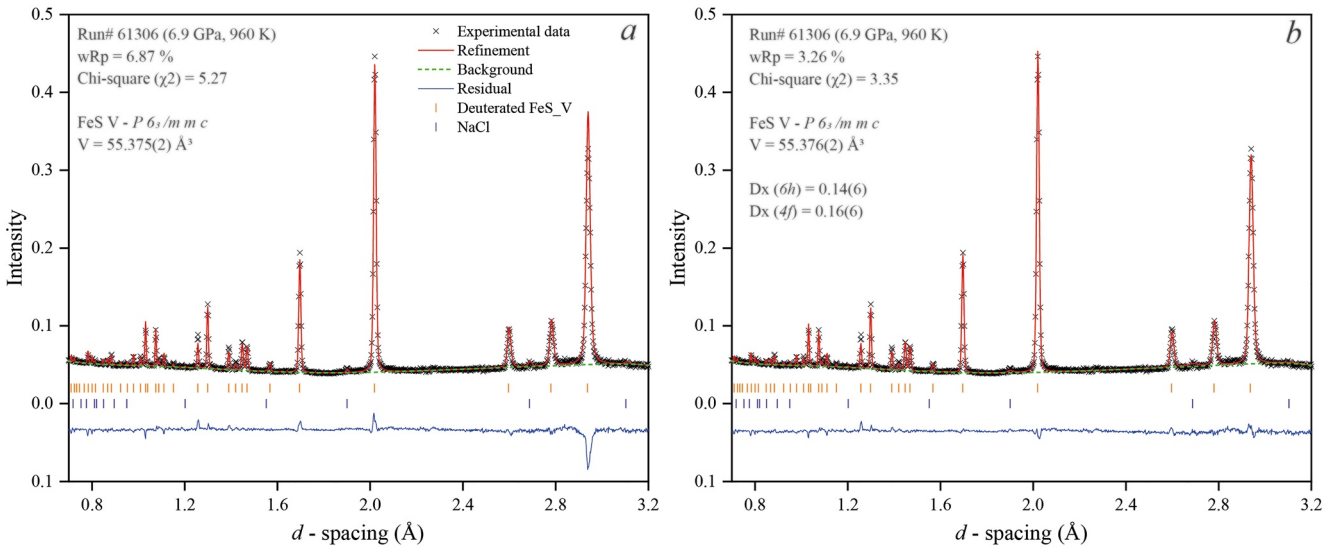

Figure 2. Rietveld structure refinements of the neutron time-of-flight data collected for the A526 experiment at 6.9 GPa and 960 K using the NiAs-type FeS V structure (hexagonal–$P6_3/mmc$, $Z = 2$) and NaCl. (a) Structural refinement with no D in the FeS V structure showing large residuals, (b) final structural model including two interstitial sites—*6h* and *4f* partially occupied by deuterium. The weighted R factor (*wRp*) of the final model in panel "b" is 3.26 %, which is a 52.5 % improvement compared to the deuterium-free model in panel "a."

phase boundaries (Figure 1). Rietveld refinements of the neutron diffraction patterns acquired at the highest *P* and *T* conditions of each experiment were performed to give insight into the deuterium position and occupancy inside the FeS V structure (as described in detail in the results section).

Pressures were determined from the unit-cell volume of NaCl obtained from the full profile analysis of the diffraction patterns. The equation-of-state of NaCl–B1 from Dorogokupets and Dewaele (2007) was used. Uncertainties in the pressure for each experiment were estimated using the error propagation equation explained in Text S1 in Supporting Information S1.

2.4. Determination of the Oxygen Fugacity Conditions Due To the Breakdown of ND_3BD_3

To examine the likely fo_2 conditions during the neutron diffraction measurements, a separate experiment was performed that replicated the sample environment of the in situ experiments but replaced the sample itself with a ferropericlase-based sliding redox sensor assemblage (Taylor et al., 1992). A 2.0 mm outer and 1.0 mm inner diameter NaCl capsule with a total sample length of 2.5 mm, was filled with two layers of deuterated ammonia borane, each of ~1.2 mm thickness, which were separated by a ~0.1 mm thick layer of $Fe_{0.2}Mg_{0.8}O$ ferropericlase, mixed with 2 wt. % of pure iron metal. The capsule was closed by a 0.5 mm thick NaCl lid. The experiment was performed using a 5,000 t Kawai-type multi-anvil press installed at the Bayerisches Geoinstitut (Frost et al., 2004) using a 18/11 set up (18 mm edge length octahedral assembly with 11 mm truncations of secondary stage tungsten carbide cubes). A stepped graphite resistive heater was used with a thermally insulating ZrO_2 sleeve. The temperature was monitored using a type D ($W_{97}Re_3$–$W_{75}Re_{25}$) thermocouple inserted axially touching a very thin (<0.2 mm) MgO disk (to prevent any damage from thermocouple to the capsule) placed on top of the capsule. The redox sensor and ammonia borane layers were equilibrated at 1300 °C and 8 GPa for 2 hr. The recovered sensor was examined using the electron probe micro analyzer and was comprised of ferropericlase with the composition $Fe_{0.13}Mg_{0.87}O$, in addition to iron metal and brucite. The fo_2 can be calculated using the equilibrium between the iron metal and ferropericlase FeO component and using thermodynamic properties given in Stagno et al. (2011). This gives a value of 1.2 ± 0.2 log units below the iron wüstite (IW) oxygen buffer.

2.5. Chemical Analyses

Three of the recovered experimental samples, A524, A526, and A527, were mounted in epoxy resin then sectioned and polished for chemical analysis with a JOEL JXA 8200 electron probe micro analyzer in wavelength dispersive mode. The sulfide assemblage was analyzed with a focused electron beam using a 20 kV acceleration voltage and 20 nA probe current. Oxygen in the sulfides was also measured using an LDE 1 (kα) crystal (Laurenz et al., 2016;

Mann et al., 2012). Counting times were 20 s for sulfur and iron and 60 s for oxygen, with half of each counting time used for the respective backgrounds. Standards employed were FeS_2 for iron and sulfur and Fe_2O_3 for oxygen. Matrix corrections were performed using the "ZAF" method. The resulting analyses yielded an average composition of 37.29 (0.19) wt. % S, 61.85 (0.23) wt. % Fe, and 0.46 (0.41) wt. % O, with no significant difference between the samples. Ignoring the negligible oxygen content, this gives the sulfide stoichiometry $Fe_{0.953(5)}S$.

3. Results

3.1. Compressibility of the FeS V Phase

During cold compression followed by heating, we observed four different high P and high T polymorphs of the $Fe_{0.95}S$ sample, described here using the following structure designations (Table 1, Figure 1, Table S3 in Supporting Information S1): FeS I (hexagonal - $\sqrt{3}a$, $2c$), FeS III (monoclinic), FeS IV (hexagonal $2a$, c) and FeS V NiAs-type structure (a, c), where a and c are the unit-cell dimensions of the NiAs-type structure used to describe the FeS polymorphs (Kusaba et al., 2000; Urakawa et al., 2004). The FeS II (MnP-type orthorhombic) structure, that has been reported between approximately 3.4 and 6.7 GPa at room-temperature (Fei et al., 1995), was not detected during our measurements. After quenching, the high-pressure FeS V phase was preserved in most of the experiments and, therefore, its volume could be studied at room temperature during decompression (Table S1, Figure S3 in Supporting Information S1). In one run (#A526), we observed that FeS V transformed to FeS IV and then FeS I upon cooling and decompression. The reason for the back-transformation from FeS V to FeS IV in this run was likely due to the relatively slow cooling rate employed (~50 K/min) across the phase boundary, as it was cooled down from 960 K at 6.9 GPa to 450 K, causing the pressure to drop to 5.8 GPa. The transformation from FeS IV to FeS I was observed during room temperature decompression between 2.8 – 1.8 GPa. A similar back-transformation has previously been observed by Kusaba et al. (2000).

The unit-cell volumes measured for FeS V during decompression (Table S1 in Supporting Information S1) and normalized with respect to the room-pressure and temperature volume, V_0 (60.08 (1) $Å^3$ - measured in this study), show an anomalous increase starting from approximately 6.5 GPa (Figure S3 in Supporting Information S1) down to room-pressure. The observed decompression curve is in good agreement with previous P–V–T trends for non-deuterated FeS samples, which implies that the sample has already lost its deuterium upon the temperature-quench. The anomalous volume change is likely due to a pressure-induced high-spin to low-spin phase transition, which must start near room-pressure but appears to be completed only above 6.5 GPa. Such a transition has been observed by means of X-ray emission spectroscopy on an FeS troilite sample (Rueff et al., 1999). These authors reported the disappearance of the low-energy satellite in the Fe $K\beta$ emission spectrum of FeS above 6.3 GPa. Changes in the electronic state of Fe in FeS at the same pressures were also reported in a high-pressure Mössbauer spectroscopy study (Kobayashi et al., 1997). Since Rueff et al. (1999) compressed troilite at room-temperature, we may expect that the FeS sample had transformed to the FeS II orthorhombic structure above 3.4 GPa (Fei et al., 1995) and, therefore, the spin transition observed at 6.3 GPa may have occurred in this phase. The low-spin state of FeS was then observed up to 11.5 GPa in the same study (Rueff et al., 1999), that is, in the stability field of the FeS III monoclinic polymorph (Nelmes et al., 1999). The pressure interval of the high-spin to low-spin transition observed from the X-ray emission spectra is very similar to the pressure at which the anomalous change in the volume of FeS V is observed in this study (Figure S3 in Supporting Information S1). This implies that the local environment of the Fe atoms in the different FeS polymorphs is seemingly independent from the precise structure topology, causing the high-spin to low-spin electronic transition to occur over a similar pressure interval. The interval between room pressure and 6.5 GPa can, therefore, be thought of as a region in which the Fe atoms in the FeS V structure have mixed configurations, of high- and low-spin states. The anomalous decrease in volume is likely due to the change in the electronic state of an increasing number of Fe atoms. The same, seemingly anomalous, volume behavior is observed in high pressure and temperature data for FeS IV and FeS V structures reported in the literature (Kusaba et al., 1998; Urakawa et al., 2004) (Figure S3 in Supporting Information S1). These results indicate that the completion of the high-spin to low-spin transition occurs at higher pressures as the temperature increases. At 1200 K, for example, the spin transition appears to be completed only above 11 GPa. Therefore, we can expect that at the target P and T of our experiments (Table 1), the electronic state of Fe in the FeS V phase consists of a mixture of high- and low-spin states.

Due to the limited pressure range investigated in this study above 6.5 GPa, it is not possible for us to determine the room temperature equation-of-state of FeS V in the low-spin state. However, our data are in good agreement with

Table 2
Results of Rietveld Structure Refinements of FeS V

	Experimental conditions			Unit-cell parameters of deuterated FeS V			Deuterium occupancies and refined parameters					
Run #	P (GPa)	T (K)	Time (hrs.)	V_{NaCl} (Å^3)	a (Å)	c (Å)	V (Å^3)	$6h$ site	$4f$ site	x apfu	Uiso	wRp (%)	χ^2
A524-1	2.3 (2)	787	7	173.24 (5)	3.4873 (1)	5.7114 (2)	60.151 (2)	0.026 (10)	0.024 (10)	0.126 (14)	0.23 (9)	3.39	5.97
A524-2	2.7 (2)	940	5	173.36 (11)	3.4908 (1)	5.7168 (2)	60.329 (2)	0.031 (12)	0.028 (11)	0.148 (17)	0.22 (7)	3.15	3.73
A526	6.9 (4)	960	11	155.1 (7)	3.3914 (1)	5.5594 (2)	55.376 (2)	0.14 (6)	0.16 (6)	0.74 (9)	0.38 (6)	3.26	3.35
A593	9.7 (4)	1,300	18	149.51 (3)	3.3667 (1)	5.5259 (3)	54.243 (3)	0.16 (6)	0.34 (14)	1.20 (16)	0.49 (9)	3.67	2.34
A527	11.4 (5)	1,250	3	144.90 (4)	3.3367 (1)	5.4696 (3)	52.739 (3)	0.11 (5)	0.23 (9)	0.81 (10)	0.5[a]	4.95	1.26

Note. Uncertainties on temperature are ±50 K, all other uncertainties are given in parentheses. Isotropic atomic displacement parameters (Uiso) are constrained to be equal for both deuterium atoms. wRp—weighted R factor, $\chi 2$—Chi-square Time indicates the diffraction pattern collection time.
[a]Not refined.

the equation-of-state reported by Urakawa et al. (2004) for the low-spin FeS V structure (note that in the original paper the low-spin state of FeS V was referred to as the high-pressure phase, HPP, whereas the high-spin state was referred to as the low-pressure phase, LPP).

3.2. Deuterium Incorporation in the FeS V Structure

With increasing temperature at high-pressure, the deuterium released from the ammonia borane (ND_3BD_3) pellets can be incorporated into the FeS V structure and it should be possible to detect its presence from the collected time-of-flight powder neutron diffraction patterns. Rietveld refinement of the diffraction pattern collected for 16 hr at 6.9 (4) GPa and 960 K (A526, Table 1) was performed using the structural model of FeS V (Brand & Briest, 1965) with Fe at the *2a* {0, 0, 0} and S at the *2c* {1/3, 2/3, 1/4} Wyckoff positions of the $P6_3/mmc$ space group. The occupancies of the two atoms were fixed to the values obtained from the chemical analysis, that is, full occupancy for the S site and 0.953 occupancy for the Fe site. The isotropic displacement parameters of both atoms were free to vary. All reflections in this diffraction pattern belonged either to the FeS V phase or to the NaCl capsule/pressure standard. No new diffraction lines were observed, indicating that the deuterium atoms randomly occupy the interstitial sites of the FeS V structure. The same observation was made by Shibazaki et al. (2011), who studied the hydrogenation of FeS V up to 16.5 GPa and 1723 K and did not report any change in symmetry for this compound based on powder X-ray diffraction patterns.

Structural refinement of the FeS V phase in sample A526 shows a large discrepancy between the observed and the calculated diffraction pattern (Figure 2-a). A difference Fourier ("DELF") map was then generated and nuclear densities (up to 0.62 e Å^{-3}) at the *6h* {x, 2x, 1/4} and *12k* {x, 2x, z} Wyckoff positions of the $P6_3/mmc$ space group were observed (Figure S4 in Supporting Information S1). Deuterium atoms were then added to the model at the two positions taken from the DELF map with a starting occupancy of 0.01. Rietveld refinements were then performed by either refining the deuterium atoms positions + occupancy or their isotropic displacement parameter (constrained to be equal to each other). During such refinements, the *6h* position was found to be very stable, while atoms in the *12k* equivalent positions became progressively closer to each other, suggesting a large dynamic disorder of the deuterium atom around an average atomic position, which can be described as a *4f* {1/3, 2/3,z} Wyckoff position. By using this *4f* position for the second deuterium atom site it was possible to refine simultaneously all atomic coordinates and isotropic displacements parameters, Uiso, (with the D atoms being constrained to have the same Uiso). The resulting final refinement (Figure 2-b) shows a substantial improvement in the fit compared to the model without deuterium (Figure 2-a), as reflected by the improvement of the "weighted R factor" (wRp) by 52.5% to a final value of 3.3% and of the Chi-square (χ^2) by 36.3% to a final value of 3.4. The calculated total deuterium content per formula unit ($FeSD_X$) is 0.74 (9), corresponding to as 1.7 (2) wt. % of D. Our final structural model for deuterated FeS V (see deposited CIF, Table 2 and Figure 3) is significantly different from what was proposed by Shibazaki et al. (2011) for hydrated FeS V based on first principle calculations. These authors suggested that octahedral interstitial sites are the most stable positions for the hydrogen atoms, whereas our results show that deuterium is instead partially occupying either a tetrahedral void (D–*4f*) or a position within the same layer defined by the S atoms (D–*6h*) (Figure 3). Both deuterium positions are much closer to the S atoms than to the Fe atoms, with the shortest S···(D–*4f*) distance equal to 1.22 (1) Å and S···(D–*6h*) distance equal to 1.23 (1) Å versus the shortest Fe···(D–*4f*) distance of 2.207 Å and Fe···(D–*6h*) distance of 1.965 Å. These short distances may be due to the strong difference in electronegativity between the S and D atoms suggesting some electronic interactions between the two.

This final deuterated model was then used to refine the other diffraction patterns collected for at least 3 hr and up to 19 hr at the different P and T conditions (Table 1). The positions of the deuterium atoms were fixed to those obtained from the refinement at 6.9 (4) GPa and 960 K to reduce the large correlations between deuterium positions, occupancies and displacement parameters, as this was the highest quality pattern due to having the largest sample size and a long collection time. The isotropic displacement parameters were constrained to be equal for the two deuterium positions. The diffraction pattern at 11.4 (5) GPa and 1250 K was collected only for 3 hours due to the occurrence of a blowout, therefore, the signal to noise ratio was not sufficient for the refinement of all parameters. For this

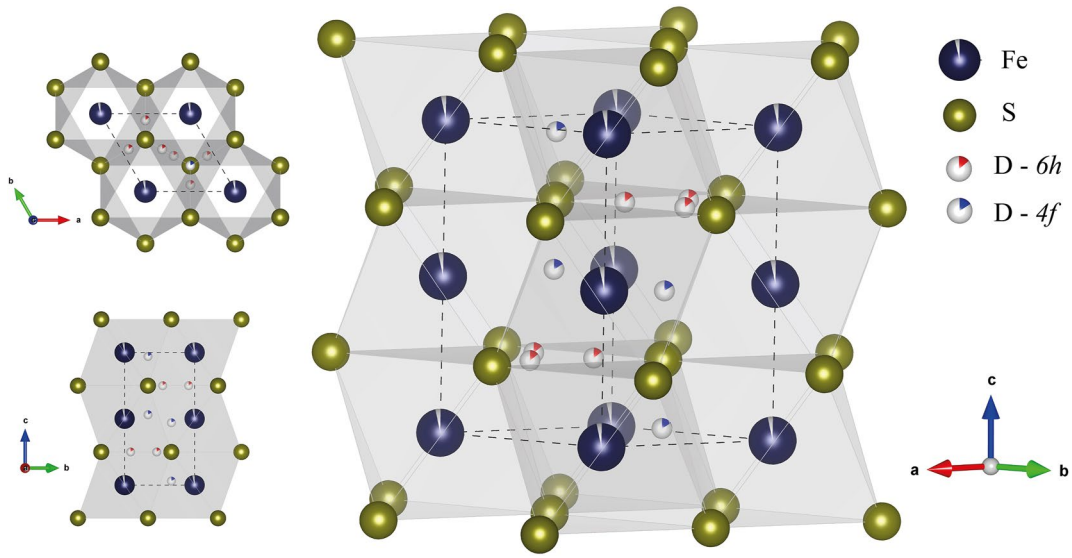

Figure 3. Final structural model of deuterated FeS V ($P6_3/mmc$, $Z = 2$) at 6.9 GPa and 960 K. Refined occupancies of D are shown in red (for *6h*) and blue (for *4f*) as a percentage of each interstitial site. The atomic coordinates for the different atoms are: Fe: {0, 0, 0}; S: {1/3, 2/3, 1/4}; D-*6h*: {0.46(2), 0.54(2), 3/4}; and D-*4f*: {1/3, 2/3, 0.03 (3)}. The dashed lines mark the unit-cell of FeS V, and the shaded polyhedra represent Fe octahedrally coordinated by S atoms. Section views along the *c*-axis and the *a*-axis of the structure are shown on the left side.

diffraction pattern, the isotropic displacement parameter of the two deuterium atoms was fixed to 0.5, that is, the same value obtained in the refinements of the diffraction pattern collected at 9.7 (4) GPa and at a similar temperature. Cubic-boron nitride (c BN) is present in the experiments at 9.7 (4) GPa and 11.4 (5) GPa (Table 1) due to the use of a smaller sample and assembly. Obtained "weighted *R* factor" (*wRp*) ranged between 3.2% and 5.0% and Chi-square (χ^2) values ranged between 1.3 and 6. Details of the structural refinements are reported in Table 2, whereas examples of the refined diffraction patterns are reported in Figure 4. The displacement parameters of deuterium appear to be correlated with temperature and are quite large for the highest-pressure experiments conducted at 1250 and 1300 K, suggesting a large dynamic disorder of the deuterium atoms.

The deuterated model of FeS V was also used for Rietveld refinement of the neutron diffraction pattern of experiment A595, where no deuterium source was added. The refinements resulted in negative displacement parameters and occupancy fraction for the deuterium atoms, confirming the absence of deuterium in the experiment and the robustness of the model for describing deuterated samples.

3.3. Volume Variation Due To Deuteration

At a given pressure and temperature, the unit-cell volume of FeS V increases because of the incorporation of deuterium into the crystal structure. For example, at 6.9 (4) GPa and 960 K, we observed a gradual increase of the unit-cell volume of FeS V over a period of 6 hr, until it became virtually constant (filled diamond symbols in Figure 5, Table S2 in Supporting Information S1). To clarify whether the cause of the unit-cell volume increase was purely due to deuteration, a second blank experiment was performed using an identical set-up but without the deuterium source; the conditions of this blank experiment were 7.3 (4) GPa and 960 K. In contrast to the deuterated experiment, after a very small volume expansion likely due to thermal adjustment of the cell assembly, there was no volumetric expansion observed over a period of 11 hr (empty diamond symbols in Figure 5). This verifies that the volume expansion (approximately 4.3 %) observed in the deuterated experiment is a result of increasing deuterium substitution. After 6 hr, the deuterated FeS V structure appears to have reached equilibrium, with a total occupancy of deuterium $X_D = 0.74$ (9) determined from Rietveld refinements (Table 2). The small difference in pressure between the non-deuterated (7.3 ± 0.4 GPa) and deuterated (6.9 ± 0.4 GPa) experiments is within the uncertainties and would produce no significant contribution to this volume difference, thus the difference in unit-cell volumes is mainly due to deuteration. The unit-cell volume expansion per one deuterium atom, ΔV(D), in the FeS V structure ($Z = 2$) can be calculated as 1.53 ± 0.16 Å^3 at 6.9 GPa, 960 K. This value is smaller compared to that proposed for Fe-metal hydrogenation (2.21 ± 0.04 Å^3—determined at 6.3 GPa and 988 K by Machida

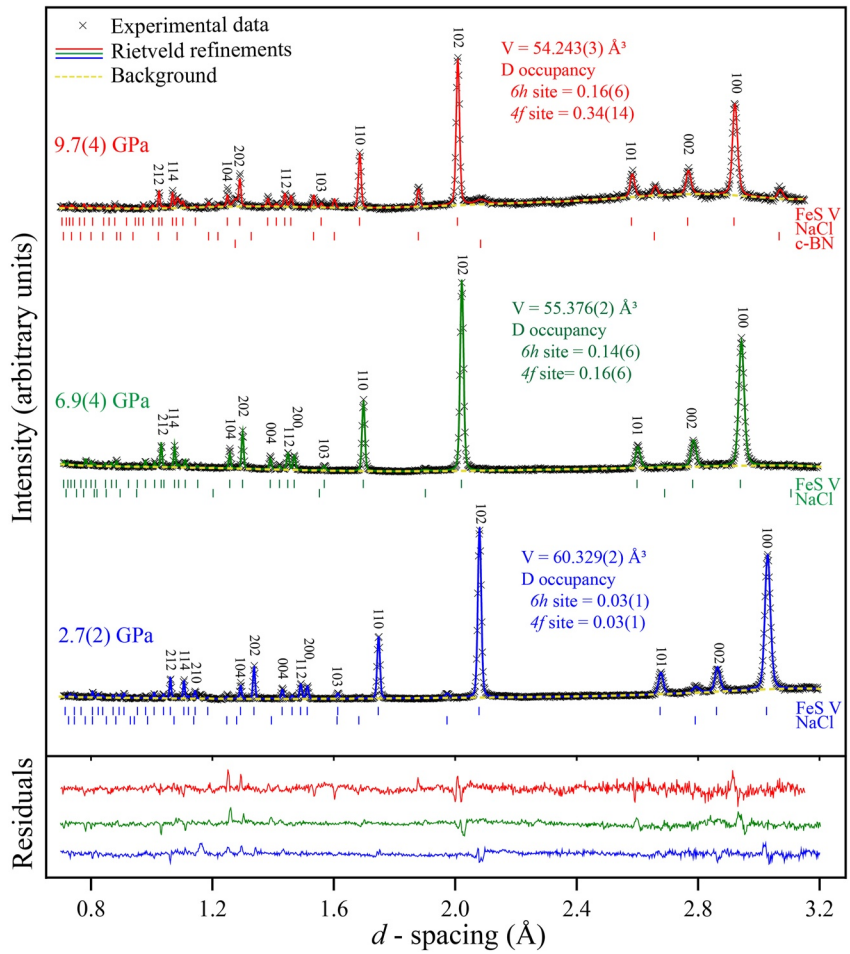

Figure 4. Rietveld refinements of neutron diffraction patterns at 2.7 (2) GPa (940 K), 6.9 (4) GPa (960 K) and 9.7 (4) GPa (1300 K). Residuals to the fit are shown at the bottom of the figure in corresponding colors for each diffraction pattern. Cubic BN is identified in the diffraction pattern at 9.7 (4) GPa, in addition to the FeS V and NaCl phases.

et al., 2014; 2.22 ± 0.36 Å^3—determined at 3.8–12.3 GPa and 900–1200 K by Ikuta et al., 2019). This is most likely because for Fe-metal, hydrogen occupies octahedral interstitial sites within layers that are not occupied by Fe, whereas for FeS V hydrogen occupies sites within layers that are also occupied by Fe and S.

The rate of deuterium uptake into the FeS V structure can be broken into three parts (Figure 5) based on the unit-cell volume expansion rate of the experiment A526 at 6.9 (4) GPa and 960 K. The first phase is completed within the time taken to heat to target temperature (approximately 15 min) and perform the first measurement (1 hr). Here, there is already a significant D content, which approaches $X_D = 0.4$ for a $FeSD_X$ stoichiometry, calculated using the unit-cell volume expansion per deuterium atom (1.53 Å^3). Next, the rate of uptake decreases significantly over the next 5–6 hr until a virtually constant D occupancy ($X_D = 0.74$) is reached (Figure 5).

In comparison with the 960 K experiment (A526), we observed faster deuterium equilibration in experiments at higher temperature (e.g., 1300 K—A593; Figure S5 in Supporting Information S1). The total D content was obtained independently using the Rietveld refinement of the diffraction pattern, indicating a total deuterium content of 2.74 wt. %, which corresponds to a D_x value of 1.20 (16) in $FeSD_X$ stoichiometry.

4. Discussion

4.1. *P-T* Behavior of the FeS V Deuterium Content and Comparison With Previous Studies

By comparing the determined deuterium contents in the experiments at 2.7 and 6.9 GPa, at 940–960 K (A524–2 and A526), it appears that there is a clear increase in deuterium substitution with increasing pressure (Figure 6).

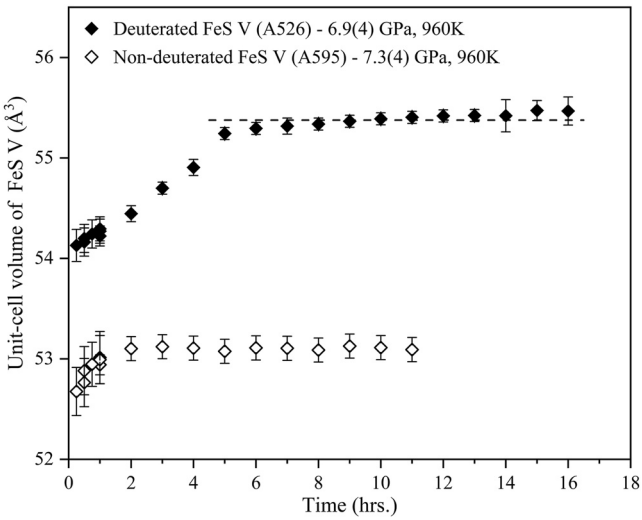

Figure 5. The unit-cell volumes of deuterated (filled diamonds–A526) and non-deuterated (empty diamonds–A595) FeS V plotted as a function of time. In the first hour, diffraction data were collected more frequently. The dashed line indicates the unit-cell volume of FeS V once the dissolution of D_2 appears to be completed (55.376 ± 0.002 Å^3) and is obtained by fitting the diffraction data over the last 11 hr of heating, (i.e., the collection time in Table 2). The average unit-cell volume of FeS V in the non-deuterated experiment is 53.111 ± 0.005 Å^3. Larger errors in the last three data points of A526 are caused by interruptions in the neutron source during the last 3 hr. All data are provided in Table S2 in Supporting Information S1.

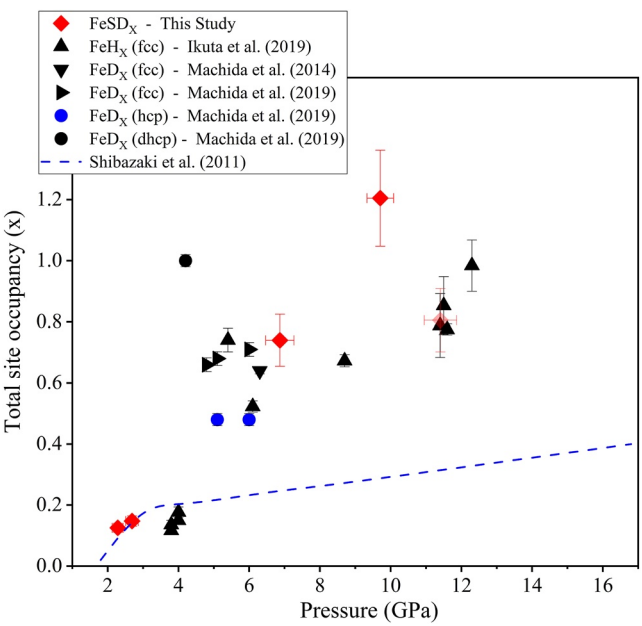

Figure 6. Total site occupancy of D/H in FeS V (red diamonds) as a function of pressure. Data from previous studies on iron hydride/deuteride are shown as triangles and circles. The occupancy of the experiment at 11.4 (5) GPa in this study (shaded red diamond symbol–#A527) may be underestimated as it was not fully equilibrated. The blue dashed line shows the increase in hydrogen occupancy with increasing pressure proposed by Shibazaki et al. (2011) using unit-cell volume relations.

The effect of temperature within the range of our experiments (787–1300 K) is harder to gauge, although with the exception of the experiment at 11.4 GPa, the results are consistent with an increase in deuterium with temperature. The experiment at 11.4 GPa (A527, Table 1), was interrupted by a blowout after the first three hours of heating, which might explain the seemingly lower than expected deuterium content as a result of the sample not fully equilibrating with D_2. The diffraction pattern is also of poorer quality than the others due to the use of a smaller sample and the short collection time. Comparing the volumes of the recovered samples, however, indicates that deuterium is lost from the FeS V sample, or strongly reduced, as the temperature is quenched at high-pressures (Figure 7). Although the room-temperature volume versus pressure curve is complicated by the change in iron spin state, it would appear that the samples quenched from high temperatures all follow a very similar decompression curve, with the non-deuterated sample also falling on this curve, albeit slightly on the lower side. This indicates that the majority of the deuterium is lost from the FeS V structure during temperature quenching, implying quite a strong temperature dependence to the deuterium content.

The strong pressure and temperature dependence of deuterium contents in solid FeS are a likely indication that an FeS liquid phase can also host at least as much hydrogen at the same conditions. The separation of an FeS liquid to the core in the final stages of core formation (Harvey et al., 2016; O'Neill, 1991; Rubie et al., 2016) may, therefore, have stripped sulfur and hydrogen from the Earth's mantle. However, quantitative estimates will require determinations of the partition coefficient of hydrogen between FeS-liquid and silicate melt as a function of P, T and oxygen fugacity. It should be possible to determine the deuterium content of an FeS-liquid, in equilibrium with a silicate melt, by cooling it to conditions where it crystallizes and then using the same in situ neutron diffraction analysis as performed here. The bulk deuterium contents would have to render FeS-liquid deuterium contents, which were at or below the saturated values determined in this study. By using a silica-rich melt it should be possible to quench and recover a glass in order to determine the coexisting deuterium content upon recovery.

In the study of Shibazaki et al. (2011), the FeS V hydrogen contents in an H_2 fluid, produced by thermal decomposition of $LiAlH_4$, were determined based on the increase in the unit-cell volume, assuming volume changes on hydrogenation based on dhcp–FeH_x measurements (Badding et al., 1991). It should be noted that such a comparison between hydrogen-bearing and hydrogen-free FeS V unit-cell volumes is complicated by the presence of the high-spin to low-spin iron transition, which prevents the application of a simple hydrogen-free FeS V equation-of-state over most of the conditions studied (Figure S2 in Supporting Information S1). Nevertheless, the hydrogen contents reported for solidus conditions by Shibazaki et al. (2011) are proposed to increase sharply between 2 and 3 GPa, from $X_H = 0.02$ to 0.2. They then increase to values of 0.4 at approximately 16.5 GPa (Figure 6). The results of our study, however, indicate, as Shibazaki et al. (2011) also suspected, that volume changes on hydrogenation from FeH_x measurements are larger than for FeS V, implying that the X_H concentrations determined by Shibazaki et al. (2011) are underestimated and may well be consistent with our study.

Iizuka-Oku et al. (2021) used neutron diffraction experiments on a multi-phase system containing Fe, S, $MgSiO_3$ and D_2O, to study the uptake of deuterium by Fe-metal and FeS over similar conditions to those in our study. They concluded that the deuterium content in FeS is negligible. However, they proposed that the presence of only small amounts of FeS (added as ~ 5 %–10 %

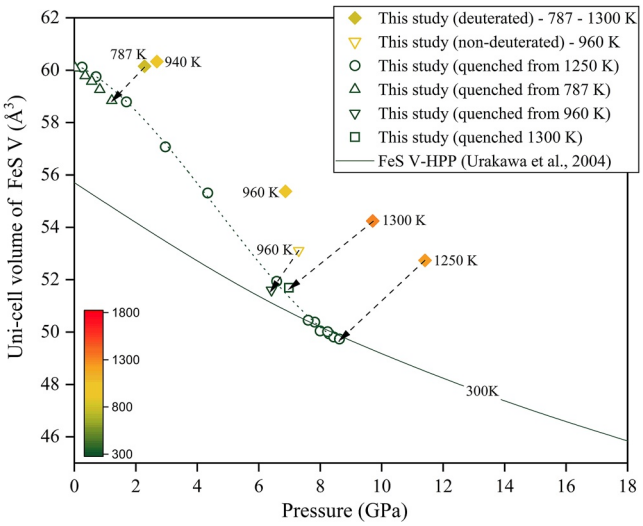

Figure 7. Absolute unit-cell volumes of samples investigated in this study plotted as a function of pressure. Open symbols indicate non-deuterated or quenched experiments from different conditions. Filled diamonds are deuterated experiments with colors indicating the temperatures, whereas the yellow upside triangle is the non-deuterated experiment at high-pressure and high-temperature. The dotted line is a guide to the eye showing the decompression trend at room-temperature. The solid line is the equation-of-state of FeS V–HPP (low spin state) at 300 K from Urakawa et al. (2004). Arrows indicate the change in volume and pressure as the samples were quenched rapidly to room-temperature.

of S powder into Fe metal powder) reduced the extent of deuteration in coexisting Fe metal (the major phase in their system). The low FeS V deuterium contents, reported in this previous study, may be due to potentially higher oxygen fugacities in the experiments, resulting from adding a D_2O source rather than D_2, giving rise to a lower deuterium fugacity (f_{D_2}). Additionally, the FeS V peaks appear to be not as strong or as well resolved as in our study, due to the patterns being dominated by fcc-Fe metal, which causes multiple peak-overlaps with FeS V, particularly at lower *d*-spacing.

Although the NiAs–type structure of FeS V (Urakawa et al., 2004) is, in principle, the same as that of dhcp-FeH_X, the accommodation of H is quite different, because in FeH_X, hydrogen is on octahedral interstitial sites, which in FeS V host the S atoms. The hydrogenation/deuteration of different iron-metal structures has been extensively examined at high pressures and temperatures using neutron diffraction experiments (Iizuka-Oku et al., 2017; Ikuta et al., 2019; Machida et al., 2014, 2019), and the H/D site occupancies obtained are compared with our values for FeS V in Figure 6. Although the measurements are performed at different temperatures, there is a general agreement in the magnitude of H/D occupancy with increasing pressure. There is also no obvious difference between studies using H or D. Although in detail there are likely to be differences in H/D accommodation due to the different structures involved and for FeS due to the high-spin low-spin transition, the general increase in pressure implies that this may be at least partly coupled to an increase in hydrogen or deuterium fugacity.

4.2. The Experimental Oxygen Fugacity and the Nature of the Coexisting Fluid Phase

Before considering the relationship between deuterium incorporation in FeS V and the deuterium fugacity, a further issue to consider is the experimental fo_2 and the composition of the coexisting fluid. The fo_2 should be controlled through the formation of a D_2-rich fluid from the breakdown of ND_3BD_3, because no other fo_2 buffering assemblage was employed. However, small amounts of adsorbed H_2O and other potential volatile impurities in the capsule and D_2 source can in principle raise the fo_2 to a level higher than that expected for a pure D_2 fluid. The tendency for oxidation to occur, likely due to absorbed water, is in fact demonstrated by the formation of small amounts of magnetite in sample A595 where no D_2 was present. To assess this a separate experiment was performed to measure the fo_2 of the source using a mixture of ferropericlase and iron metal, which gave a value of 1.2 ± 0.2 log units below the IW oxygen buffer at 8 GPa and 1300 °C. It is possible to make a simple calculation for the H_2 content of an O–H fluid at these conditions, which will not be significantly different to the D_2 content (Tkacz & Litwiniuk, 2002), assuming ideal mixing and the equilibrium:

$$H_2 + \frac{1}{2}O_2 = H_2O \tag{2}$$

with values for the equilibrium coefficient *K* from Holland and Powell (2011), where:

$$K = \frac{f_{H_2O}}{f_{H_2}.\left(f_{O_2}\right)^{0.5}} \tag{3}$$

Assuming ideal mixing in the H_2–H_2O fluid then:

$$f_{H_2} = P_T.X_{H_2}.\varnothing_{H_2} \tag{4}$$

where P_T is the total pressure, X_{H_2} the mole fraction and $\varnothing_{H_2}$ is the fugacity coefficient of pure H_2, determined here using the equations of state of Belonoshko and Saxena (1991). A similar expression can be written for H_2O and when this and Equation 4 are substituted into Equation 3 and the constraint that $X_{H_2} = 1 - X_{H_2O}$ is applied, then the combined expression can be solved to give X_{H_2} as a function of fo_2. This is shown by the black curve in Figure 8, which indicates that at the experimental conditions and ΔIW −1.2, the fluid is calculated to be only

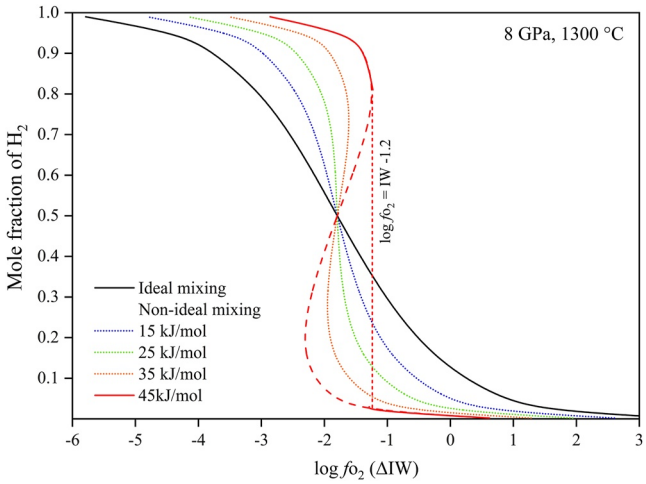

Figure 8. The proportion of H_2 in an H_2–H_2O fluid as a function of oxygen fugacity relative to the iron–wüstite oxygen buffer (ΔIW), calculated for the indicated pressure and temperature condition. The calculation uses the equation-of-state of Belonoshko and Saxena (1991), assuming both ideal mixing of H_2 and H_2O in the fluid (solid black curve) and for a series of non-ideal mixing Margules interaction parameters. As non-ideality increases, a back bend in the proportion of H_2 occurs, which indicates regions where immiscible H_2 and H_2O–rich fluids coexist at the same oxygen fugacity. For an interaction parameter of 45 kJ/mol this coexistence occurs at an oxygen fugacity consistent with the experimentally measured value. The vertical red dotted line connects the coexisting immiscible fluid compositions at this oxygen fugacity.

36 mol % H_2. The relatively high fo_2 obtained in the experiments is, therefore, apparently inconsistent with a D_2-dominated fluid, which should comprise more than 90% of the fluid only at ΔIW −4, according to this ideal mixing model.

It is unlikely that adsorbed H_2O would be sufficient to dominate over the significant amount of stoichiometric D_2 that would be released by ND_3BD_3, and it is more likely that the assumption of H_2–H_2O ideal mixing in the calculation is incorrect. Evidence for this comes from the observation of H_2–H_2O immiscibility at high pressures and temperatures (Bali et al., 2013), where separate, nearly pure, H_2 and H_2O fluids were found to coexist at conditions of IW. The critical temperature for closure of this solvus was found to increase quite strongly between 1.5 and 2.7 GPa, from approximately 800 to 1000 °C. Some idea of the consequences of H_2–H_2O non-ideal mixing can be obtained by including a further activity coefficient, $\gamma_{H_2}^{H_2-H_2O}$, in Equation 4, which can in turn be described using a Margules interaction parameter, W, that is,:

$$RT \ln \gamma_{H_2}^{H_2-H_2O} = W_{H_2-H_2O}\left(1 - X_{H_2}\right)^2 \quad (5)$$

where R is the gas constant and T is temperature. As shown in Figure 8, increasing non-ideality reduces the range of fo_2 over which H_2O-rich fluids reduce to H_2-rich fluids. An H_2-dominated fluid can be stabilized at an fo_2 of ΔIW −1.2, coexisting with an immiscible H_2O dominated fluid, if the interaction parameter is approximately 45 kJ/mol. This is slightly larger than the value required to explain the observations of Bali et al. (2013) between 1 and 3 GPa, but the value should increase with pressure in line with the increase in the critical temperature. This indicates that the fo_2 determined in this study upon D_2 release is quite consistent with the observations of H_2O–H_2 immiscibility of Bali et al. (2013). In detail, the non-ideal interaction parameter may be asymmetric and require a more complex P and T fitting. This should not, however, change the main implications from Figure 8, that H_2-dominated fluids can be stable at higher fo_2 than might be expected. Because the transition between H_2O and H_2 dominated fluids occurs over a smaller fo_2 range, the mole fraction of H_2 in the H_2O-rich fluid that dominates at higher oxygen fugacities is most likely lower than would be expected if ideal mixing is assumed.

4.3. A Model for the Deuterium Content of FeS V and Extrapolation to Mantle Conditions

As there are two FeS molecules in the FeS V unit-cell, then there are two *4f* deuterium sites and three *6h* sites that could potentially be occupied by deuterium for the FeS stoichiometry. However, the set of three *6h* sites are unlikely to be all deuterated at the same time, due to their close proximity, and it seems more reasonable to assume that only one of these sites can be deuterated. For each FeS this means a total possible occupancy of three deuterium atoms (one in the *6h* position and two in the *4f* position), that is, a fictive fully deuterated endmember of $FeSD_3$. Assuming that the ND_3BD_3 source produces a pure D_2 fluid, which the calculations in the previous section seem to support, then the deuteration can be considered as,

$$FeS\square_3 + \frac{3}{2}D_2 = FeSD_3 \quad (6)$$

where □ indicates the vacant interstitial sites. If for simplicity we assume disorder over all three sites, then we can relate the concentration of deuterium, to the deuterium fugacity and the standard state Gibbs free energy change, ΔG^o, of reaction 6 through:

$$\ln\left(\frac{a\mathrm{FeSD}_3}{a\mathrm{FeS}\square_3 \cdot \left[f_{D_2}\right]^{\frac{3}{2}}}\right) = \frac{-\Delta G^o}{RT} \quad (7)$$

Assuming ideal mixing of D in the FeS V structure, the activities are given by:

$$a\mathrm{FeSD}_3 = \left[\frac{X_\mathrm{D}}{3}\right]^3 \tag{8}$$

and

$$a\mathrm{FeS}\square_3 = \left[\frac{3 - X_\mathrm{D}}{3}\right]^3 \tag{9}$$

where X_D is the deuterium content per FeS formula unit, given in Table 2. The experimental data can then be fitted by taking hydrogen fugacities (assumed to be identical to deuterium fugacities) from Belonoshko and Saxena (1991), and fitting ΔG^o as $\Delta H^\mathrm{o} - T\Delta S^\mathrm{o} + P\Delta V^\mathrm{o}$. If the anomalous 11.4 GPa data is not considered, the fitting parameters are $\Delta H^\mathrm{o} = 64.8 \pm 13$ kJ/mol, $\Delta S^\mathrm{o} = -154 \pm 19$ J/(mol.K) and $\Delta V^\mathrm{o} = 0.66 \pm 0.11$ J/bar. Given that four data points are being fit with three parameters it is perhaps not surprising that the fit is very good and the largest residual in X_D is only 0.04. The ΔV^o is larger than the value of 0.3 J/bar that can be estimated from the volume change on deuteration, ΔV(D), determined in this study (Figure 5), however, and if the ΔV^o is fixed at 0.3 J/bar, the largest X_D residual increases to 0.22. It may not be reasonable to assume ideal mixing of D in the vacant sites, however, and if we choose a single site Margules mixing parameter of −1.2 kJ/mol then the resulting fitting parameters give a ΔV^o that is in reasonable agreement with the experimental determination, that is, $\Delta H^\mathrm{o} = 112 \pm 17$ kJ/mol, $\Delta S^\mathrm{o} = -145 \pm 14$ J/(mol.K) and $\Delta V^\mathrm{o} = 0.35 \pm 0.14$ J/bar. Although these models are almost certainly oversimplified and would require far more data to become robust, they do allow a basic qualitative exploration of how D/H uptake in FeS V is likely to change under different conditions. First, both models predict that if equilibrium is maintained, the D content should drop to low levels on quenching to room-temperature at high-pressure, in agreement with the quenched FeS V unit-cell volumes shown in Figure 7.

Second, by considering that

$$f_{\mathrm{H}_2} = P_T.\varnothing_{\mathrm{H}_2}.X_{\mathrm{H}_2}.\gamma_{\mathrm{H}_2}^{\mathrm{H}_2-\mathrm{H}_2\mathrm{O}} \tag{10}$$

as in Equation 4, that is, adding a further activity coefficient to describe non-ideal mixing between H_2O and H_2 as defined in Equation 5 and consistent with the observations of Bali et al. (2013), then the effect of lower H_2, fugacities, can be explored on the equilibrium FeS V hydrogen contents. As Fe-Ni-rich monosulfides are the dominant inclusion found in diamonds, the relevant conditions to explore this relationship are those at which diamonds exist in the subcratonic lithospheric mantle. For a typical cratonic geotherm, with temperatures of 1300 °C at 6.5 GPa that is, approximately 200 km depth, then FeS V would be subsolidus (Zhang & Hirschmann, 2016) and in a pure H_2 fluid the two models predict an FeS X_H of 0.8–0.87, which is equivalent to approximately 1 wt. % hydrogen in the structure. However, diamond bearing peridotite mantle xenoliths at these conditions record typical values of fo_2, relative to the fayalite-magnetite-quartz oxygen buffer (FMQ), of ΔFMQ −3 ± 1 or ΔIW +1.8. As carbon at these conditions is mainly in the form of diamond (Shirey et al., 2013), an O–H mixing calculation similar to that described in the previous section, at ΔFMQ of −3, predicts a H_2 fluid activity (i.e., $X_{\mathrm{H}_2}.\gamma_{\mathrm{H}_2}^{\mathrm{H}_2-\mathrm{H}_2\mathrm{O}}$) of 0.02, which results in a predicted FeS X_H of 0.15–0.24 or 1,700–2,700 ppm hydrogen in the structure, depending on which FeS V fitting model is used. The hydrogen content would be half this value at ΔFMQ of −2. Of course, hydrogen activities may have been much lower than this during diamond formation and FeS inclusion capture, depending on the nature of the medium from which they are formed. This relatively simple calculation, however, appears to indicate that significant hydrogen contents could be accommodated by FeS inclusions in diamonds. If such diamonds were then brought to the surface, the reduction in temperature and pressure would cause the FeS inclusions to exsolve H_2, which could of course react with the diamond to also produce CH_4. The analysis of these components might give the false impression that the inclusions were captured at very reducing conditions. A further possibility is that this loss of hydrogen from the inclusions upon decompression, may cause hydrogen embrittlement of the diamond, as often encountered in diamond anvil cell experiments on hydrogen (Eremets & Trojan, 2009), which may then play a role in the development of the rosette like fracture systems often observed around sulfide inclusions in diamonds (Harris, 1972). This may also be promoted by the strong volume expansion that would occur due to the FeS V iron spin transition, as indicated in Figure 7.

It is also possible to estimate how much hydrogen could be stored in FeS monosulfide phases within the bulk mantle rocks at the base of the cratonic lithosphere. If these rocks contain on average approximately 400 ppm sulfur (Gehlen, 1992) accommodated at these conditions in FeS V and were in equilibrium with an O-H fluid at $\Delta FMQ = -3$, 2–3 ppm H_2 could be hosted by sulfides in the bulk rock, which is equivalent to 16–26 ppm H_2O. This value would decrease at higher oxygen fugacities and at shallower depths in the cratonic lithosphere. At greater depths the oxygen fugacity of the mantle is expected to decrease and the FeS V phase would also become molten promoting likely higher hydrogen contents in the sulfide phase, although this remains to be experimentally tested.

5. Summary

Time-of-flight powder neutron diffraction measurements at pressures up to 11.4 GPa and temperatures to 1300 K were performed to study the solubility of deuterium in the NiAs-structured FeS V polytype of pyrrhotite. Thermal decomposition of ND_3BD_3 was used to create a D_2 dominated fluid in the multi-anvil experiments. Rietveld structure refinements indicated the partial occupancy of deuterium on two normally unoccupied sites in the structure at Wyckoff positions *6h*: {0.46(2), 0.54(2), 3/4} and *4f*: {1/3, 2/3, 0.03 (3)} at high-pressure and temperature conditions, with the latter being more dominant.

The incorporation of deuterium in the crystal structure increases the unit-cell volume of FeS V by 4.3% at 6.9 GPa and 960 K and the unit-cell volume expansion per deuterium atom, $\Delta V(D)$, is 1.53 ± 0.16 Å^3. This is smaller compared to that previously reported for the hydrogenation of Fe-metal phases at similar conditions (2.21 ± 0.04 Å^3—Machida et al., 2014). The structural model indicates that both deuterium sites are closer to the S atoms than to the Fe atoms, such that S and D may be covalently bonded, which may explain the smaller $\Delta V(D)$ value compared to Fe-metal phases. Previously reported hydrogen contents in FeS V, by means of X-ray diffraction volume relations are likely underestimated, due to the use of a $\Delta V(H)$ value estimated from results on hydrogenated Fe-metal phases (Shibazaki et al., 2011). The deuterium dissolved in FeS V at high-temperature is mainly lost during temperature quenching at high-pressure, as indicated by the decrease in unit-cell volumes of the quenched experiments.

Refinements of the collected diffraction patterns indicate that the D content in FeS V increases with both pressure and temperature. The total deuterium content, x in FeSDx, increases from 0.126 (14) at 2.3 GPa and 787 K to 1.20 (16) at 9.7 GPa and 1300 K. A comparison between FeSDx and FeHx/FeDx measurements at similar conditions shows that there is a general similarity in the magnitude of H/D occupancy with increasing pressure. Therefore, sulfide segregation toward the end of core formation (O'Neill, 1991) may be a plausible mechanism by which H_2 could have been stripped from the mantle, possibly facilitating oxidation of the mantle by H_2O, although this remains to be tested in detail.

A parallel multi-anvil experiment was conducted to determine the oxygen fugacity of samples exposed to the D_2 fluid produced by the breakdown of ND_3BD_3, indicating an oxygen fugacity of 1.2 ± 0.2 log units below the iron wüstite (IW) oxygen buffer. This is much higher than would be expected for an O-H fluid dominated by H_2 if ideal mixing of H_2–H_2O is assumed. It is consistent, however, with the degree of non-ideal mixing implied by the observation of immiscibility between H_2 and H_2O-rich fluids (Bali et al., 2013).

The D_2 solubilites are fitted to a thermodynamic model which confirms that FeS V hydrogen contents should drop to low levels on temperature quenching at high-pressure. The model is extrapolated to the lower H_2 fugacities consistent with the higher oxygen fugacities at the base of the cratonic lithosphere. At these conditions FeS V could still contain significant amounts of hydrogen, in the range of 1,700–2,700 ppm. Loss of hydrogen from diamond hosted FeS V during decompression could play a role in the development of the rosette like fracture systems often observed around sulfide inclusions in diamonds (Harris, 1972). Based on an average mantle sulfur content of 400 ppm (Gehlen, 1992), then at the base of the cratonic lithosphere a bulk mantle H_2 content of 2–3 ppm could be hosted by mantle sulfides. At greater depths lower oxygen fugacities and melting of FeS V may lead to higher hydrogen contents in sulfides.

Finally, it may be possible to study the partitioning of deuterium between sulfide melts and silicate melts and minerals at highpressure and temperature conditions, by quenching the sulfide melts to temperatures where the deuterium content of the crystallized FeS V assemblage is still below the D_2 solubility. The deuterium contents

in the quenched FeS V assemblage would then be determined using the same type of in situ neutron diffraction measurement, whereas the silicates would be recovered to room-pressure for analysis.

Data Availability Statement

The final structural model for deuterated FeS V (CIF file) in this study is deposited on figshare repository and is available online at (Abeykoon et al., 2023) via https://doi.org/10.6084/m9.figshare.21820677.v2.

Acknowledgments
We would like to thank Raphael Njul, Alexander Rother and Heinz Fischer for their technical assistance. Dr. Takanori Hattori is thanked for scheduling the experiments at J-PARC (proposal number 2019B0117) and for valuable discussion. Dr. Florian Heidelbach and Dr. Shin Ozawa are thanked for their help with the analysis of some experimental samples and we thank Dr. Nicolas Walte for constructive discussions. We thank, for the constructive reviews and suggestions from the associate editor, two anonymous reviewers, and for editorial handling Yves Bernabe. This project was conducted as a part of the "Deep volatile cycles"—International Research Training Group funded by the German Research Foundation (Deutsche Forschungsgemeinschaft—DFG, GRK 2156/1) and through DFG Grant FR1555/11. Open Access funding enabled and organized by Projekt DEAL.

References

Abeykoon, S., Howard, C., Dominijanni, S., Eberhard, L., Kurnosov, A., Frost, D. J., et al. (2023). Deuterium content and site occupancy in iron sulfide at high pressure and temperature determined using in situ neutron diffraction measurements - The final structural model for deuterated FeS V – CIF (Version 2) [Dataset]. figshare. https://doi.org/10.6084/m9.figshare.21820677.v2

Antonov, V. E., Cornell, K., Fedotov, V. K., Kolesnikov, A. I., Ponyatovsky, E. G., Shiryaev, V. I., & Wipf, H. (1998). Neutron diffraction investigation of the dhcp and hcp iron hydrides and deutendes. *Journal of Alloys and Compounds*, *264*(1–2), 214–222. https://doi.org/10.1016/S0925-8388(97)00298-3

Badding, J. V., Hemley, R. J., & Mao, H. K. (1991). High-pressure chemistry of hydrogen in metals: In situ study of iron hydride. *Science*, *253*(5018), 421–424. https://doi.org/10.1126/science.253.5018.421

Bali, E., Audétat, A., & Keppler, H. (2013). Water and hydrogen are immiscible in Earth's mantle. *Nature*, *495*(7440), 220–222. https://doi.org/10.1038/nature11908

Belonoshko, A., & Saxena, S. K. (1991). A molecular dynamics study of the pressure-volume-temperature properties of supercritical fluids: II. CO_2, CH_4, CO, O_2, and H_2. *Geochimica et Cosmochimica Acta*, *55*(11), 3191–3208. https://doi.org/10.1016/0016-7037(91)90483-L

Bondar, D., Fei, H., Withers, A. C., Ishii, T., Chanyshev, A., & Katsura, T. (2021). A simplified rapid-quench multi-anvil technique. *Review of Scientific Instruments*, *92*(11), 113902. https://doi.org/10.1063/5.0062525

Brand, P., & Briest, J. (1965). Das Quasi-Binäre system NiAs-Ni1,5Sn. *Zeitschrift für Anorganische und Allgemeine Chemie*, *337*(3–4), 209–213. https://doi.org/10.1002/zaac.19653370314

Clesi, V., Bouhifd, M. A., Bolfan-Casanova, N., Manthilake, G., Schiavi, F., Raepsaet, C., et al. (2018). Low hydrogen contents in the cores of terrestrial planets. *Science Advances*, *4*(3), e1701876. https://doi.org/10.1126/sciadv.1701876

Dawidowski, J., Granada, J. R., Santisteban, J. R., Cantargi, F., & Palomino, L. A. R. (2013). Neutron scattering lengths and cross sections. In *Experimental methods in the physical sciences* (Vol. 44). Elsevier Inc. https://doi.org/10.1016/B978-0-12-398374-9.09989-7

Delano, J. W. (2001). Redox history of the Earth's interior since ~3900 Ma: Implications for prebiotic molecules. *Origins of Life and Evolution of the Biosphere*, *31*(4–5), 311–341. https://doi.org/10.1023/A:1011895600380

Dorogokupets, P. I., & Dewaele, A. (2007). Equations of state of MgO, Au, Pt, NaCl-B1, and NaCl-B2: Internally consistent high-temperature pressure scales. *High Pressure Research*, *27*(4), 431–446. https://doi.org/10.1080/08957950701659700

Eremets, M. I., & Trojan, I. A. (2009). Evidence of maximum in the melting curve of hydrogen at megabar pressures. *JETP Letters*, *89*(4), 174–179. https://doi.org/10.1134/S0021364009040031

Fei, Y., Charles, T., Prewitt, C. T., Mao, H., & Bertka, C. M. (1995). Structure and density of FeS at high pressure and high temperature and the internal structure of Mars. *Science*, *268*(5219), 1892–1894. https://doi.org/10.1126/science.268.5219.1892

Fei, Y., Prewitt, C. T., Frost, D. J., Parise, J. B., & Brister, K. (1998). Structures of FeS polymorphs at high pressure and temperature. *The Review of High Pressure Science and Technology*, *7*, 55–58. https://doi.org/10.4131/jshpreview.7.55

Frost, D. J., Poe, B. T., Trønnes, R. G., Liebske, C., Duba, A., & Rubie, D. C. (2004). A new large-volume multianvil system. *Physics of the Earth and Planetary Interiors*, *143*(1–2), 507–514. https://doi.org/10.1016/j.pepi.2004.03.003

Fukai, Y., Mori, K., & Shinomiya, H. (2003). The phase diagram and superabundant vacancy formation in Fe-H alloys under high hydrogen pressures. *Journal of Alloys and Compounds*, *348*(1–2), 105–109. https://doi.org/10.1016/S0925-8388(02)00806-X

Fukai, Y., & Suzuki, T. (1986). Iron-water reaction under high pressure and its implication in the evolution of the Earth. *Journal of Geophysical Research*, *91*(B9), 9222–9230. https://doi.org/10.1029/JB091iB09p09222

Harris, J. W. (1972). Black material on mineral inclusions and in internal fracture planes in diamond. *Contributions to Mineralogy and Petrology*, *35*(1), 22–33. https://doi.org/10.1007/BF00397374

Harvey, J., Warren, J. M., & Shirey, S. B. (2016). Mantle sulfides and their role in Re–Os and Pb isotope geochronology. *Reviews in Mineralogy and Geochemistry*, *81*(1), 579–649. https://doi.org/10.2138/rmg.2016.81.10

Hattori, T., Sano-Furukawa, A., Arima, H., Komatsu, K., Yamada, A., Inamura, Y., et al. (2015). Design and performance of high-pressure PLANET beamline at pulsed neutron source at J-PARC. *Nuclear Instruments and Methods in Physics Research Section A: Accelerators, Spectrometers, Detectors and Associated Equipment*, *780*, 55–67. https://doi.org/10.1016/j.nima.2015.01.059

Hernlund, J., Leinenweber, K., Locke, D., & Tyburczy, J. A. (2006). A numerical model for steady-state temperature distributions in solid-medium high-pressure cell assemblies. *American Mineralogist*, *91*(2–3), 295–305. https://doi.org/10.2138/am.2006.1938

Holland, T. J. B., & Powell, R. (2011). An improved and extended internally consistent thermodynamic dataset for phases of petrological interest, involving a new equation of state for solids. *Journal of Metamorphic Geology*, *29*(3), 333–383. https://doi.org/10.1111/j.1525-1314.2010.00923.x

Iizuka-Oku, R., Gotou, H., Shito, C., Fukuyama, K., Mori, Y., Hattori, T., et al. (2021). Behavior of light elements in iron-silicate-water-sulfur system during early Earth's evolution. *Scientific Reports*, *11*(1), 12632. https://doi.org/10.1038/s41598-021-91801-3

Iizuka-Oku, R., Yagi, T., Gotou, H., Okuchi, T., Hattori, T., & Sano-Furukawa, A. (2017). Hydrogenation of iron in the early stage of Earth's evolution. *Nature Communications*, *8*(1), 14096. https://doi.org/10.1038/ncomms14096

Ikuta, D., Ohtani, E., Sano-Furukawa, A., Shibazaki, Y., Terasaki, H., Yuan, L., & Hattori, T. (2019). Interstitial hydrogen atoms in face-centered cubic iron in the Earth's core. *Scientific Reports*, *9*(1), 7108. https://doi.org/10.1038/s41598-019-43601-z

Kasting, J. F. (1993). Earth's early atmosphere. *Science*, *259*(5097), 920–926. https://doi.org/10.1126/science.11536547

Kiseeva, E. S., & Wood, B. J. (2013). A simple model for chalcophile element partitioning between sulphide and silicate liquids with geochemical applications. *Earth and Planetary Science Letters*, *383*, 68–81. https://doi.org/10.1016/j.epsl.2013.09.034

Kobayashi, H., Sato, M., Kamimura, T., Sakai, M., Onodera, H., Kuroda, N., & Yamaguchi, Y. (1997). The effect of pressure on the electronic states of FeS and Fe_7S_8 studied by Mössbauer spectroscopy. *Journal of Physics: Condensed Matter*, *9*(2), 515–527. https://doi.org/10.1088/0953-8984/9/2/019

Kusaba, K., Syono, Y., Kikegawa, T., & Shimomura, O. (1998). High pressure and temperature behavior of FeS. *Journal of Physics and Chemistry of Solids*, *59*(6–7), 945–950. https://doi.org/10.1016/S0022-3697(98)00015-8

Kusaba, K., Utsumi, W., Yamakata, M., Shimomura, O., & Syono, Y. (2000). Second-order phase transition of FeS under high pressure and temperature. *Journal of Physics and Chemistry of Solids*, *61*(9), 1483–1487. https://doi.org/10.1016/S0022-3697(00)00005-6

Larson, A. C., & Von Dreele, R. B. (2004). *General structure analysis system (GSAS)*. Los Alamos National Laboratory Report LAUR, University of California.

Laurenz, V., Rubie, D. C., Frost, D. J., & Vogel, A. K. (2016). The importance of sulfur for the behavior of highly-siderophile elements during Earth's differentiation. *Geochimica et Cosmochimica Acta*, *194*, 123–138. https://doi.org/10.1016/j.gca.2016.08.012

Machida, A., Saitoh, H., Hattori, T., Sano-Furukawa, A., Funakoshi, K., Sato, T., et al. (2019). Hexagonal close-packed iron hydride behind the conventional phase diagram. *Scientific Reports*, *9*(1), 12290. https://doi.org/10.1038/s41598-019-48817-7

Machida, A., Saitoh, H., Sugimoto, H., Hattori, T., Sano-Furukawa, A., Endo, N., et al. (2014). Site occupancy of interstitial deuterium atoms in face-centred cubic iron. *Nature Communications*, *5*(1), 5063. https://doi.org/10.1038/ncomms6063

Malavergne, V., Bureau, H., Raepsaet, C., Gaillard, F., Poncet, M., Surblé, S., et al. (2019). Experimental constraints on the fate of H and C during planetary core-mantle differentiation. Implications for the Earth. *Icarus*, *321*, 473–485. https://doi.org/10.1016/j.icarus.2018.11.027

Mann, U., Frost, D. J., Rubie, D. C., Becker, H., & Audétat, A. (2012). Partitioning of Ru, Rh, Pd, Re, Ir and Pt between liquid metal and silicate at high pressures and high temperatures - Implications for the origin of highly siderophile element concentrations in the Earth's mantle. *Geochimica et Cosmochimica Acta*, *84*, 593–613. https://doi.org/10.1016/j.gca.2012.01.026

Nelmes, R. J., McMahon, M. I., Belmonte, S. A., & Parise, J. B. (1999). Structure of the high-pressure phase III of iron sulfide. *Physical Review B*, *59*(14), 9048–9052. https://doi.org/10.1103/PhysRevB.59.9048

Nishihara, Y., Doi, S., Kakizawa, S., Higo, Y., & Tange, Y. (2020). Effect of pressure on temperature measurements using WRe thermocouple and its geophysical impact. *Physics of the Earth and Planetary Interiors*, *298*, 106348. https://doi.org/10.1016/j.pepi.2019.106348

Nylén, J., Sato, T., Soignard, E., Yarger, J. L., Stoyanov, E., & Häussermann, U. (2009). Thermal decomposition of ammonia borane at high pressures. *Journal of Chemical Physics*, *131*(10), 104506. https://doi.org/10.1063/1.3230973

Okuchi, T. (1997). Hydrogen partitioning into molten iron at high pressure: Implications for Earth's core. *Science*, *278*(5344), 1781–1784. https://doi.org/10.1126/science.278.5344.1781

O'Neill, H. St. C. (1991). The origin of the moon and the early history of the Earth-A chemical model. Part 2: The Earth. *Geochimica et Cosmochimica Acta*, *55*(4), 1159–1172. https://doi.org/10.1016/0016-7037(91)90169-6

Piet, H., Leinenweber, K., Greenberg, E., Prakapenka, V. B., & Shim, S. H. (2021). Effects of hydrogen on the phase relations in Fe-FeS at pressures of Mars-sized bodies. *Journal of Geophysical Research: Planets*, *126*(11), e2021JE006942. https://doi.org/10.1029/2021JE006942

Ringwood, A. E. (1977). Composition of the core and implications for origin of the Earth. *Geochemical Journal*, *11*(3), 111–135. https://doi.org/10.2343/geochemj.11.111

Rubie, D. C. (1999). Characterising the sample environment in multianvil high-pressure experiments. *Phase Transitions*, *68*(3), 431–451. https://doi.org/10.1080/01411599908224526

Rubie, D. C., Laurenz, V., Jacobson, S. A., Morbidelli, A., Palme, H., Vogel, A. K., & Frost, D. J. (2016). Highly siderophile elements were stripped from the Earth's mantle by iron sulfide segregation. *Science*, *353*(6304), 1141–1144. https://doi.org/10.1126/science.aaf6919

Rueff, J. P., Kao, C. C., Struzhkin, V. V., Badro, J., Shu, J., Hemley, R. J., & Mao, H. K. (1999). Pressure-induced high-spin to low-spin transition in FeS evidenced by X-ray emission spectroscopy. *Physical Review Letters*, *82*(16), 3284–3287. https://doi.org/10.1103/PhysRevLett.82.3284

Sakamaki, K., Takahashi, E., Nakajima, Y., Nishihara, Y., Funakoshi, K., Suzuki, T., & Fukai, Y. (2009). Melting phase relation of FeHx up to 20 GPa: Implication for the temperature of the Earth's core. *Physics of the Earth and Planetary Interiors*, *174*(1–4), 192–201. https://doi.org/10.1016/j.pepi.2008.05.017

Sano-Furukawa, A., Hattori, T., Arima, H., Yamada, A., Tabata, S., Kondo, M., et al. (2014). Six-axis multi-anvil press for high-pressure, high-temperature neutron diffraction experiments. *Review of Scientific Instruments*, *85*(11), 113905. https://doi.org/10.1063/1.4901095

Sears, V. F. (1992). Neutron scattering lengths and cross sections. *Neutron News*, *3*(3), 26–37. https://doi.org/10.1080/10448639208218770

Sharp, Z. D., McCubbin, F. M., & Shearer, C. K. (2013). A hydrogen-based oxidation mechanism relevant to planetary formation. *Earth and Planetary Science Letters*, *380*, 88–97. https://doi.org/10.1016/j.epsl.2013.08.015

Shibazaki, Y., Ohtani, E., Terasaki, H., Tateyama, R., Sakamaki, T., Tsuchiya, T., & Funakoshi, K. (2011). Effect of hydrogen on the melting temperature of FeS at high pressure: Implications for the core of Ganymede. *Earth and Planetary Science Letters*, *301*(1–2), 153–158. https://doi.org/10.1016/j.epsl.2010.10.033

Shirey, S. B., Cartigny, P., Frost, D. J., Keshav, S., Nestola, F., Nimis, P., et al. (2013). Diamonds and the geology of mantle carbon. *Reviews in Mineralogy and Geochemistry*, *75*(1), 355–421. https://doi.org/10.2138/rmg.2013.75.12

Solozhenko, V. L., Turkevich, V. Z., & Holzapfel, W. B. (1999). Refined phase diagram of boron nitride. *Journal of Physical Chemistry B*, *103*(15), 2903–2905. https://doi.org/10.1021/jp984682c

Stagno, V., Tange, Y., Miyajima, N., McCammon, C. A., Irifune, T., & Frost, D. J. (2011). The stability of magnesite in the transition zone and the lower mantle as function of oxygen fugacity. *Geophysical Research Letters*, *38*(19), L19309. https://doi.org/10.1029/2011GL049560

Stähler, S. C., Khan, A., Banerdt, W. B., Lognonné, P., Giardini, D., Ceylan, S., et al. (2021). Seismic detection of the Martian core. *Science*, *373*(6553), 443–448. https://doi.org/10.1126/science.abi7730

Tagawa, S., Sakamoto, N., Hirose, K., Yokoo, S., Hernlund, J., Ohishi, Y., & Yurimoto, H. (2021). Experimental evidence for hydrogen incorporation into Earth's core. *Nature Communications*, *12*(1), 2588. https://doi.org/10.1038/s41467-021-22035-0

Taylor, J. R., Wall, V. J., & Pownceby, M. I. (1992). The calibration and application of accurate redox sensors. *American Mineralogist*, *77*(3–4), 284–295.

Tenner, T. J., Hirschmann, M. M., Withers, A. C., & Hervig, R. L. (2009). Hydrogen partitioning between nominally anhydrous upper mantle minerals and melt between 3 and 5 GPa and applications to hydrous peridotite partial melting. *Chemical Geology*, *262*(1–2), 42–56. https://doi.org/10.1016/j.chemgeo.2008.12.006

Tkacz, M., & Litwiniuk, A. (2002). Useful equations of state of hydrogen and deuterium. *Journal of Alloys and Compounds*, *330–332*, 89–92. https://doi.org/10.1016/S0925-8388(01)01488-8

Toby, B. H. (2001). EXPGUI, a graphical user interface for GSAS. *Journal of Applied Crystallography*, *34*(2), 210–213. https://doi.org/10.1107/S0021889801002242

Urakawa, S., Someya, K., Terasaki, H., Katsura, T., Yokoshi, S., Funakoshi, K., et al. (2004). Phase relationships and equations of state for FeS at high pressures and temperatures and implications for the internal structure of Mars. *Physics of the Earth and Planetary Interiors*, *143–144*, 469–479. https://doi.org/10.1016/j.pepi.2003.12.015

von Gehlen, K. (1992). Sulfur in the Earth's mantle—A review. In M. Schidlowski, S. Golubic, M. M. Kimberley, D. M. McKirdy, & P. A. Trudinger (Eds.), *Early organic evolution* (pp. 359–366). Springer. https://doi.org/10.1007/978-3-642-76884-2_27

Wood, B. J., & Halliday, A. N. (2005). Cooling of the Earth and core formation after the giant impact. *Nature*, *437*(7063), 1345–1348. https://doi.org/10.1038/nature04129

Zhang, Z., & Hirschmann, M. M. (2016). Experimental constraints on mantle sulfide melting up to 8 GPa. *American Mineralogist*, *101*(1), 181–192. https://doi.org/10.2138/am-2016-5308